Rayleigh–Bénard instability in a vertical cylinder with a vertical magnetic field

By B. C. HOUCHENS, L. MARTIN WITKOWSKI†
AND J. S. WALKER

Department of Mechanical and Industrial Engineering, University of Illinois,
1206 West Green St., Urbana, IL 61801, USA

This paper presents two linear stability analyses for an electrically conducting liquid contained in a vertical cylinder with a thermally insulated vertical wall and with isothermal top and bottom walls. There is a steady uniform vertical magnetic field. The first linear stability analysis involves a hybrid approach which combines an analytical solution for the Hartmann layers adjacent to the top and bottom walls with a numerical solution for the rest of the liquid domain. The second linear stability analysis involves an asymptotic solution for large values of the Hartmann number. Numerically accurate predictions of the critical Rayleigh number can be obtained for Hartmann numbers from zero to infinity with the two solutions presented here and a previous numerical solution which gives accurate results for small values of the Hartmann number.

1. Introduction

During the growth of semiconductor crystals from a body of heated liquid, hydrodynamic instabilities often lead to non-axisymmetric flows, and the associated non-axisymmetric mass transfer produces non-uniform distributions of additives in the crystals. Since molten semiconductors are good electrical conductors, a magnetic field can be applied during crystal growth to stabilize the liquid motion and to produce better crystals. The extensive use of magnetic stabilization in crystal growth has motivated a number of recent studies of the linear stability of buoyant and thermocapillary convection with uniform steady magnetic fields. In all of these studies, numerically accurate or grid-independent results could only be obtained for small values of the Hartmann number, $Ha = BR(\sigma/\mu)^{1/2}$, where B is the magnetic flux density of the applied magnetic field and R is the radius of the liquid domain, while σ and μ are the electrical conductivity and dynamic viscosity of the liquid. For most crystal-growth processes with magnetic stabilization, the values of Ha are at least an order of magnitude larger than the largest values for numerically accurate results in these recent studies. Here we present methods which give numerically accurate results for values of Ha from zero to infinity.

Prange *et al.* (1999) presented a linear stability analysis for the thermocapillary convection in a cylindrical liquid bridge between two isothermal circular disks at different temperatures and with a steady uniform axial magnetic field. For a Prandtl number of 0.02 and an axial length equal to R, they presented a thorough documentation of the number of grid points in the radial and axial directions needed to

† Present address: LIMSI, BP 133, F 91403 Orsay Cedex, France.

achieve grid-independent predictions of the critical Reynolds number. For $Ha = 10$ and $Ha = 15$, numerical accuracy was achieved with a 30×80 grid (radial × axial) and a 35×100 grid, respectively. For $Ha = 20$, they could not obtain accurate results even with a 40×120 grid. They stated that finer grids were not possible with their computational resources, and they only presented stability results for $Ha \leqslant 15$. The numerical resolution problems were concentrated in the eigenvalue problem for the small perturbation variables. They presented accurate numerical results for the steady axisymmetric base flow for $Ha \leqslant 200$. The instability of the steady, axisymmetric thermocapillary convection treated by Prange *et al.* (1999) is fundamentally different from the Rayleigh–Bénard instability treated here, but we mention their work in order to illustrate that different types of linear stability analyses are limited to small values of Ha because of numerical resolution problems.

Gelfgat & Bar-Yoseph (2001) considered small, planar perturbations to the steady, planar buoyant convection in a rectangle with thermally insulated top and bottom walls and with isothermal endwalls at different temperatures. They included a steady uniform magnetic field whose direction could be varied between vertical and horizontal. They stated: 'A convergence study involving different values of the Hartmann number and different orientations of the magnetic field shows that accurate modeling of the electromagnetic effects requires better numerical resolution than one which suffices for different cases of pure buoyancy convection'. They indicate that more resolution is needed because the Hartmann layers become thin for rather small values of Ha, but still play an important role in the instability. They only presented results for $Ha \leqslant 20$, where their Ha is based on the height of the rectangle.

Touihri, Ben Hadid & Henry (1999*b*) presented a linear stability analysis for the problem treated here, namely a vertical circular cylinder with a thermally insulated vertical wall, with isothermal top and bottom walls at different temperatures and with a steady uniform axial magnetic field. They only presented results for $Ha \leqslant 15$. They based their Hartmann and Rayleigh numbers on the diameter of the cylinder, while we use the radius R, so we will convert their values to our definitions throughout this paper. While they did not discuss any numerical limitations, their contours of the radial velocity in the critical mode reveal that the Hartmann layers adjacent to the top and bottom walls are already quite thin for $Ha = 15$.

Dold & Benz (1995) presented experimental temperature measurements for liquid gallium contained in a vertical cylinder with a thermally insulated vertical wall, with isothermal top and bottom walls at different temperatures, and with an axial length which was twice the diameter. For a Rayleigh number of 9844, the temperature at a fixed point in the liquid fluctuated chaotically without a magnetic field and was constant with a magnetic field for which $Ha = 212$. The present paper concerns the primary instability with transition from a stagnant fluid to a steady flow. The experimental measurements of Dold & Benz (1995) are concerned with a secondary instability with transition to unsteady flow. Their results show that for $Ha = 212$, the critical Rayleigh number for the secondary instability is greater than 9844. However, their results do not provide any information about the primary instability since their constant temperature at a fixed point would occur for either a stagnant fluid or a steady flow.

Many researchers have studied the Rayleigh–Bénard instability in a vertical cylinder without a magnetic field. Three numerical treatments of the primary and secondary instabilities without a magnetic field were presented by Neumann (1990), Wanschura, Kuhlmann & Rath (1996) and Touihri, Ben Hadid & Henry (1999*a*). Many researchers have also treated the effects of a steady uniform magnetic field on three-dimensional

instabilities in buoyant convection in other geometries. For example, Hurle, Jakeman & Johnson (1974) presented an experimental study of the instabilities in a horizontal rectangular prism with isothermal ends at different temperatures, with the other four walls thermally insulated and with a uniform horizontal magnetic field which was parallel to the isothermal endwalls. Juel *et al.* (1999) presented numerical solutions for the same problem. Ben Hadid, Henry & Touihri (1997) presented numerical solutions for the instability in a horizontal circular cylinder with a thermally insulated cylindrical wall, with isothermal endwalls at different temperatures and with a steady uniform vertical magnetic field.

For the thermocapillary instability or for the buoyant instability with an essentially horizontal base-state temperature gradient, there are numerical accuracy issues for both the base state and the small perturbation. The results of Prange *et al.* (1999) for the thermocapillary instability indicate that the limitation to small values of Ha arises from resolution problems for the small perturbation and not for the base flow. Since the base state for the Rayleigh–Bénard problem consists of a stagnant liquid and a linear temperature variation, the only numerical accuracy issues concern the perturbation.

The present paper represents an extension of the work of Touihri *et al.* (1999*b*) who treated the Rayleigh–Bénard instability in a vertical cylinder with a vertical magnetic field and with $Ha \leqslant 15$. Our paper presents linear stability analyses for larger values of Ha. Our first linear stability analysis involves a hybrid approach which combines (i) an analytical solution for the Hartmann layers with $O(Ha^{-1})$ thickness adjacent to the top and bottom walls, and (ii) a numerical solution for the rest of the liquid domain. By eliminating the need to resolve the thin Hartmann layers numerically, the hybrid solution gives grid-independent results with reasonable computational resources up to roughly $Ha = 500$. We have extended the fully numerical approach of Touihri *et al.* (1999*b*) to $Ha = 40$–80, depending on the aspect ratio of the cylinder, thus demonstrating that $Ha = 15$ did not represent any limit of accuracy for their fully numerical solution. There is excellent agreement between the predictions of the hybrid approach and of the fully numerical approach for a range of values of Ha for each of the two aspect ratios considered here. Our second linear stability analysis involves an asymptotic solution for $Ha \gg 1$. This analysis shows that the critical Rayleigh number varies as $Ha^{3/2}$ for $Ha \gg 1$. There is excellent agreement between the hybrid and asymptotic solutions for a range of values of Ha. With our hybrid and asymptotic solutions and with the fully numerical solution of Touihri *et al.* (1999*b*), accurate results can be obtained for values of Ha from zero to infinity.

2. Problem formulation

In addition to the applied magnetic field, there is an induced magnetic field produced by the electric currents in the liquid. The characteristic ratio of the induced to applied magnetic fields is the magnetic Reynolds number, $Rm = \mu_p \sigma U_c R$, where μ_p is the magnetic permeability of the liquid and U_c is a characteristic velocity for the liquid motion. Here the liquid is stagnant in the base state and the linear stability analysis involves a small perturbation, so it is difficult to define a suitable U_c. However, for all laminar flows in crystal growth processes, Rm is so small that the induced magnetic field can be neglected. Baumgartl & Müller (1992) showed that the time-dependent induced magnetic field may be important for the turbulent flows in some very large crystal-growth processes.

For the cylindrical coordinates r, θ, z, the z-axis lies along the vertical centreline

of the cylinder and the origin lies at the centre of the cylinder, and r and z are normalized by R. We assume that all walls are electrical insulators. The dimensionless boundary conditions are

$$\boldsymbol{v} = 0, \quad j_r = 0, \quad \frac{\partial T}{\partial r} = 0 \quad \text{at} \quad r = 1, \tag{1a–c}$$

$$\boldsymbol{v} = 0, \quad j_z = 0, \quad T = \mp\tfrac{1}{2} \quad \text{at} \quad z = \pm b, \tag{1d–f}$$

where $\boldsymbol{v}$ is the liquid velocity normalized by v/R, $\boldsymbol{j}$ is the electric current density normalized by $\sigma v B/R$, and T is the deviation of the temperature from the average temperature, normalized by (ΔT), which is the temperature difference between the isothermal top and bottom walls. Here $2b$ is the dimensionless height of the cylinder and v is the kinematic viscosity of the liquid. With the Boussinesq approximation and with the neglect of the induced magnetic field, the dimensionless governing equations are

$$\frac{\partial \boldsymbol{v}}{\partial t} + (\boldsymbol{v} \cdot \boldsymbol{\nabla})\boldsymbol{v} = -\boldsymbol{\nabla} p + \frac{Ra}{Pr} T\hat{z} + Ha^2(\boldsymbol{j} \times \hat{z}) + \nabla^2 \boldsymbol{v}, \tag{2a}$$

$$\boldsymbol{\nabla} \cdot \boldsymbol{v} = 0, \quad \boldsymbol{j} = -\boldsymbol{\nabla}\phi + \boldsymbol{v} \times \hat{z}, \quad \boldsymbol{\nabla} \cdot \boldsymbol{j} = 0, \tag{2b–d}$$

$$\frac{\partial T}{\partial t} + \boldsymbol{v} \cdot \boldsymbol{\nabla} T = \frac{1}{Pr}\nabla^2 T, \tag{2e}$$

where t is time normalized by R^2/v, p is the deviation of the pressure from the hydrostatic pressure for a uniform density ρ, normalized by $\rho v^2/R^2$, and ϕ is the electric potential function normalized by vB. Here

$$Ra = \frac{g\beta(\Delta T)R^3}{v\kappa}, \quad Pr = \frac{v}{\kappa} \tag{3a,b}$$

are the Rayleigh and Prandtl numbers, while $\hat{z}$ is a unit vector in the z-direction, $g = 9.81\,\text{m s}^{-2}$, β is the volumetric expansion coefficient of the liquid, and κ is the thermal diffusivity of the liquid.

For the linear stability analysis, we introduce

$$T = -\frac{z}{2b} + Pr\,\varepsilon\,Re[\exp(\lambda t + im\theta)T_1(r,z)] \tag{4a}$$

for the temperature, we introduce the form

$$v_r = \varepsilon\,Re[\exp(\lambda t + im\theta)v_{r1}(r,z)] \tag{4b}$$

for v_r, v_z, p and j_θ, and we introduce the form

$$v_\theta = \varepsilon\,Re[\exp(\lambda t + im\theta)iv_{\theta 1}(r,z)] \tag{4c}$$

for v_θ, ϕ, j_r and j_z. Here $\lambda = \lambda_r + i\lambda_i$ is the possibly complex eigenvalue, m is the real integer azimuthal wavenumber, and the modal functions with the subscript 1 may be complex. The i is included in (4c) so that all modal functions are real if λ is real, and Pr is included in (4a) so that Pr drops out of the problem if λ for the critical mode is zero. Neglecting $O(\varepsilon^2)$ terms, equations (2) become

$$\lambda v_{r1} = -\frac{\partial p_1}{\partial r} + Ha^2 j_{\theta 1} + \nabla^2 v_{r1} - \frac{v_{r1}}{r^2} + \frac{2m}{r^2}v_{\theta 1}, \tag{5a}$$

$$\lambda v_{\theta 1} = -\frac{m}{r}p_1 - Ha^2 j_{r1} + \nabla^2 v_{\theta 1} - \frac{v_{\theta 1}}{r^2} + \frac{2m}{r^2}v_{r1}, \tag{5b}$$

$$\lambda v_{z1} = -\frac{\partial p_1}{\partial z} + RaT_1 + \nabla^2 v_{z1}, \tag{5c}$$

$$\frac{\partial v_{r1}}{\partial r} + \frac{v_{r1}}{r} - \frac{m}{r}v_{\theta 1} + \frac{\partial v_{z1}}{\partial z} = 0, \tag{5d}$$

$$j_{r1} = -\frac{\partial \phi_1}{\partial r} + v_{\theta 1}, \quad j_{\theta 1} = \frac{m}{r}\phi_1 - v_{r1}, \tag{5e,f}$$

$$j_{z1} = -\frac{\partial \phi_1}{\partial z}, \quad \frac{\partial j_{r1}}{\partial r} + \frac{j_{r1}}{r} + \frac{m}{r}j_{\theta 1} + \frac{\partial j_{z1}}{\partial z} = 0, \tag{5g,h}$$

$$\lambda Pr T_1 - \frac{v_{z1}}{2b} = \nabla^2 T_1, \tag{5i}$$

where now

$$\nabla^2 = \frac{\partial^2}{\partial r^2} + \frac{1}{r}\frac{\partial}{\partial r} - \frac{m^2}{r^2} + \frac{\partial^2}{\partial z^2}. \tag{5j}$$

With the addition of a subscript 1 to each dependent variable, the homogeneous boundary conditions (1*a*)–(1*e*) still apply, while (1*f*) is replaced by

$$T_1 = 0 \quad \text{at} \quad z = \pm b. \tag{6}$$

First we describe our duplication of the fully numerical solution of Touihri *et al.* (1999*b*). Equations (5*d*) and (5*b*) were used to eliminate $v_{\theta 1}$ and p_1, respectively. After these substitutions, (5*a*) includes the terms $Ha^2(\partial j_{r1}/\partial r + j_{r1}/r + mj_{\theta 1}/r)$ which are replaced by $-Ha^2\partial j_{z1}/\partial z$ because of (5*h*). Finally (5*e*)–(5*g*) were used to eliminate j_{r1}, $j_{\theta 1}$ and j_{z1}, leaving four modal functions, v_{r1}, v_{z1}, T_1 and ϕ_1. We used a Chebyshev spectral collocation method to reduce the homogeneous differential equations and boundary conditions to a matrix eigenvalue problem, which was solved using the rgg subroutine in the EISPACK library. In order to ensure that the Chebyshev polynomial representation of each modal function matched the correct Taylor series expansions in r, we used the form

$$r^{(m-1)}\sum_L \sum_N A_{LN} T_{2L}(r)T_N(z/b) \tag{7a}$$

for v_{r1} and the form

$$r^m \sum_L \sum_N B_{LN} T_{2L}(r)T_N(z/b) \tag{7b}$$

for v_{z1}, T_1 and θ_1, where $T_k(x) = \cos[k\arccos(x)]$ are the Chebyshev polynomials. Our pseudospectral method is quite different from the isoparametric spectral element method used by Touihri *et al.* (1999*b*), but the results are the same for $Ha < 15$ and for both aspect ratios considered here. For each value of Ha and for a range of integer values for m, we increased Ra until one eigenvalue had $\lambda_r = 0$ for each value of m. The critical Rayleigh number Ra_{cr} is the minimum of the values of Ra for $\lambda_r = 0$ and for all values of m.

Next we present our hybrid approach which combines an analytical solution for the Hartmann layers which have an $O(Ha^{-1})$ thickness and which lie adjacent to the top and bottom walls at $z = \pm b$, and a numerical solution for the rest of the liquid domain. As the value of Ha is increased, Hartmann layers develop near the walls which are perpendicular to the applied magnetic field. Hartmann layers have a simple, local, exponential structure, which satisfies the boundary conditions (1*d*) and (1*e*) at $z = \pm b$, and which matches any values of v_{r1} and $v_{\theta 1}$ in the rest of the domain, provided

the solution in the rest of the domain satisfies the Hartmann conditions (Moreau 1990). The Hartmann conditions come from matching the analytical solutions in the Hartmann layers and the variables in the rest of the domain. Many researchers have presented solutions for Hartmann layers and for Hartmann conditions, and we use the Hartmann conditions presented by Hunt & Ludford (1968),

$$v_{z1} \pm Ha^{-1} \left[\frac{\partial v_{r1}}{\partial r} + \frac{v_{r1}}{r} - \frac{m}{r} v_{\theta 1} \right] = 0 \quad \text{at} \quad z = \pm b, \qquad (8a)$$

$$j_{z1} \pm Ha^{-1} \left[\frac{\partial v_{\theta 1}}{\partial r} + \frac{v_{\theta 1}}{r} - \frac{m}{r} v_{r1} \right] = 0 \quad \text{at} \quad z = \pm b. \qquad (8b)$$

For the domain excluding the Hartmann layers, there are no boundary conditions on v_{r1} and $v_{\theta 1}$ at $z = \pm b$, but if these velocities involve a divergence in the plane at $z = \pm b$, then conservation of mass inside each Hartmann layer gives an $O(Ha^{-1})v_{z1}$ flow into or out of the Hartmann layer, often called Hartmann pumping; and if these velocities involve a swirl in the plane at $z = \pm b$, the conservation of electric current inside each Hartmann layer gives an $O(Ha^{-1})j_{z1}$ flow into or out of the Hartmann layer, often called the Hartmann current. The development of the Hartmann layers as Ha is increased implies that the viscous diffusion of momentum in the z-direction is negligible outside the Hartmann layers. Therefore the two important features of the hybrid approach are: (i) the terms $\partial^2 \boldsymbol{v}_1 / \partial z^2$ in $\nabla^2 \boldsymbol{v}_1$ in (5a), (5b) and (5c) are neglected, and (ii) the Hartmann conditions (8a) and (8b) are applied at $z = \pm b$ instead of the boundary conditions (1d) and (1e). Since we drop the no-slip conditions $v_{r1} = v_{\theta 1} = 0$ at $z = \pm b$, we must drop the viscous terms $\partial^2 \boldsymbol{v}_1 / \partial z^2$ in $\nabla^2 \boldsymbol{v}_1$ for a well-posed problem. Since the region treated numerically includes both the inviscid core and the boundary layer at $r = 1$, the radial derivatives in $\nabla^2 \boldsymbol{v}_1$ must be kept. The viscous terms involving m from the azimuthal derivatives in $\nabla^2 \boldsymbol{v}_1$ are kept because it is not *a priori* obvious that m does not become large for $Ha \gg 1$. The numerical solution makes no distinction between the core and the boundary layer at $r = 1$, so that it is important that this layer is numerically resolved. With the grid used for all of our hybrid-solution results, there are collocation points at $r = 0.99745, 0.98982, 0.97715, 0.95949$ and 0.93695, so that the boundary layer at $r = 1$ is well resolved for the values of Ha considered here. The jump in T_1 across each Hartmann layer is at most $O(Ha^{-3})$, so that the boundary conditions (6) are still applied. The rest of the numerical solution for the domain excluding the Hartmann layers is identical to the fully numerical solution.

Finally we present our asymptotic solutions for $Ha \gg 1$. It is difficult to determine the dimensions of the subregions for $Ha \gg 1$ from (5) because there are nine variables. It is easy to combine (5) into a few higher-order equations governing fewer variables. The key equations have the same form, $\lambda \nabla^2 \phi_1 = \nabla^4 \phi_1 - Ha^2 \partial^2 \phi_1 / \partial z^2$, plus lower-order coupling terms with the other variables. This is an equation for the axial vorticity, which is given by $\nabla^2 \phi_1$. From this and similar equations, it is clear that the boundary layers at $z = \pm b$ have an $O(Ha^{-1})$ thickness and the boundary layer at $r = 1$ has an $O(Ha^{-1/2})$ thickness. In other buoyant-convection problems with strong magnetic fields, different boundary-layer thicknesses arise from the nonlinear inertial terms or from different relationships between the geometry of the boundary, the magnetic-field direction and the gravitational direction or from different electrical conductivities of the walls. However, the subregions shown in figure 1 are the only ones for the present problem. The subregions are the core region (c), the primary Hartmann layers (h) which have an $O(Ha^{-1})$ thickness and which lie between the core and the top and bottom at $z = \pm b$, the parallel layer (p) which has an $O(Ha^{-1/2})$
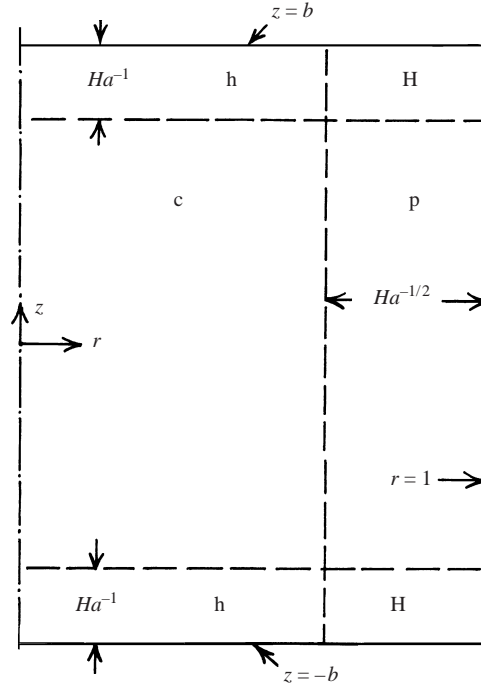
FIGURE 1. Subregions of the liquid domain for $Ha \gg 1$: c = core, h = primary Hartmann layer, p = parallel layer and H = secondary Hartmann layer.

thickness and which lies between the core and the vertical wall at $r = 1$, and the secondary Hartmann layers (H) which have $\Delta r = O(Ha^{-1/2})$, $\Delta z = O(Ha^{-1})$ and which lie between the parallel layer and the top and bottom at $z = \pm b$. For both the fully numerical solution and the hybrid solution, all eigenvalues λ are real, as expected for the Rayleigh–Bénard problem (Touihri *et al.* 1999*a*, *b*). Thus the instability always leads to a steady flow which is either axisymmetric ($m = 0$) or non-axisymmetric ($m \geqslant 1$), and $\lambda = 0$ for the critical mode. For the asymptotic solution, we set $\lambda = 0$ with no loss of generality. First we consider the relationships between variables in the core and parallel layer without specifying orders of magnitude.

In the core, the viscous terms in equations (5*a*)–(5*c*) are $O(Ha^{-2})$ smaller than the other terms and are neglected, so that (5*a*), (5*b*), (5*c*), (5*e*) and (5*f*) give

$$j_{r1} = -Ha^{-2}\frac{m}{r}p_1, \quad j_{\theta 1} = Ha^{-2}\frac{\partial p_1}{\partial r}, \quad \frac{\partial p_1}{\partial z} = RaT_1, \tag{9a–c}$$

$$v_{r1} = \frac{m}{r}\phi_1 - Ha^{-2}\frac{\partial p_1}{\partial r}, \quad v_{\theta 1} = \frac{\partial \phi_1}{\partial r} - Ha^{-2}\frac{m}{r}p_1. \tag{9d, e}$$

Substitution of (9*a*), (9*b*) and (5*g*) into (5*h*) gives

$$\frac{\partial^2 \phi_1}{\partial z^2} = 0, \tag{10}$$

while substitution of (9*d*), (9*e*) and (5*g*) into the Hartmann condition (8*b*) gives

$$\frac{\partial \phi_1}{\partial z} = \pm Ha^{-1}\left[\frac{\partial^2 \phi_1}{\partial r^2} + \frac{1}{r}\frac{\partial \phi_1}{\partial r} - \frac{m^2}{r^2}\phi_1\right] \quad \text{at} \quad z = \pm b. \tag{11}$$

The solution of (10) and (11) is $\phi_1 = 0$, so that ϕ_1 is at most $O(Ha^{-2}\boldsymbol{v}_1)$ in the core. Substitution of (9c)–(9e) and (5i) into (5d) gives

$$\frac{\partial v_{z1}}{\partial z} = -RaHa^{-2} \left[\frac{\partial T_1}{\partial z} + \frac{1}{2b} \int v_{z1} \, dz \right]. \tag{12}$$

Equations (5i) and (12) indicate that if $Ra = O(Ha^2)$, then v_{z1} in the core and the base-state axial temperature gradient produce a perturbation temperature T_1 which leads to a buoyancy force to produce this v_{z1} in the core.

For the parallel layer, we introduce the stretched coordinate $\xi = Ha^{1/2}(r-1)$. Equation (5d) indicates that v_{r1} is $O(Ha^{-1/2})$ smaller than $v_{\theta 1}$ and v_{z1}, while (5h) indicates that j_{r1} is $O(Ha^{-1/2})$ smaller than $j_{\theta 1}$ and j_{z1}. Thus the leading-order terms in equations (5) are

$$j_{\theta 1} = Ha^{-3/2}\frac{\partial p_1}{\partial \xi}, \quad j_{r1} = -Ha^{-2}mp_1 + Ha^{-1}\frac{\partial^2 v_{\theta 1}}{\partial \xi^2}, \tag{13a,b}$$

$$\frac{\partial p_1}{\partial z} = RaT_1 + Ha\frac{\partial^2 v_{z1}}{\partial \xi^2}, \quad Ha^{1/2}\frac{\partial v_{r1}}{\partial \xi} - mv_{\theta 1} + \frac{\partial v_{z1}}{\partial z} = 0, \tag{13c,d}$$

$$v_{\theta 1} = Ha^{1/2}\frac{\partial \phi_1}{\partial \xi}, \quad v_{r1} = m\phi_1 - j_{\theta 1}, \quad j_{z1} = -\frac{\partial \phi_1}{\partial z}, \tag{13e–g}$$

$$Ha^{1/2}\frac{\partial j_{r1}}{\partial \xi} + mj_{\theta 1} + \frac{\partial j_{z1}}{\partial z} = 0, \quad -\frac{v_{z1}}{2b} = Ha\frac{\partial^2 T_1}{\partial \xi^2} + Ha^{1/2}\frac{\partial T_1}{\partial \xi}. \tag{13h,i}$$

Substitution of (13a), (13b), (13e) and (13g) into (13h) gives

$$\frac{\partial^4 \phi_1}{\partial \xi^4} - \frac{\partial^2 \phi_1}{\partial z^2} = 0. \tag{14}$$

Substitution of (13a), (13e) and (13f) into (13d) gives

$$Ha^{-1}\frac{\partial^2 p_1}{\partial \xi^2} = \frac{\partial v_{z1}}{\partial z}. \tag{15}$$

The boundary conditions (1a)–(1c) become

$$m\phi_1 - Ha^{-3/2}\frac{\partial p_1}{\partial \xi} = \frac{\partial \phi_1}{\partial \xi} = v_{z1} = 0 \quad \text{at} \quad \xi = 0, \tag{16a–c}$$

$$\frac{\partial^3 \phi_1}{\partial \xi^3} - Ha^{-3/2}mp_1 = \frac{\partial T_1}{\partial \xi} = 0 \quad \text{at} \quad \xi = 0. \tag{16d,e}$$

Equations (13c) and (15) show that the buoyancy force produces a velocity v_{z1} inside the parallel layer which is $O(RaHa^{-1}T_1)$. Thus (13i) and (16e) show that

$$\lim_{\xi \to -\infty} \frac{\partial T_1}{\partial \xi} = O(RaHa^{-2}T_1). \tag{17}$$

This temperature gradient enters the 2-inner, 2-outer matching of T_1 in the core and T_1 in the parallel layer, which implies that $O(Ha^{-1/2}T_1) = O(RaHa^{-2}T_1)$ or $Ra = O(Ha^{3/2})$.

Chandrasekhar (1961) treated the Rayleigh–Bénard instability in a liquid layer between two infinite horizontal isothermal walls with a uniform vertical magnetic field. He showed that $Ra_{cr} = O(Ha^2)$, which agrees with our conclusion from (12)

that $Ra_{cr} = O(Ha^2)$ for a self-sustained instability in the core. The lower value of $Ra_{cr} = O(Ha^{3/2})$ arises from the perturbation velocity and the associated convective heat transfer inside the parallel layer. In the core or in an infinite horizontal layer, any horizontal component of vorticity drives a circulation of electric current, and the ratio of the joulean dissipation in the current circulation to the viscous dissipation in the vorticity is $O(Ha^2)$. Inside the parallel layer, the electrically insulating vertical wall blocks radial electric currents, so that a radial component of vorticity inside the parallel layer leads to a circulation of electric current whose joulean dissipation is only $O(Ha^{3/2})$ times the viscous dissipation in the vorticity. This suggests three remarks about other situations. First, for the Rayleigh–Bénard instability in a cylinder with an electrically conducting vertical wall, radial electric currents are not blocked, so that $Ra_{cr} = O(Ha^2)$ for $Ha \gg 1$. Second, if only axisymmetric perturbations with $m = 0$ are considered, there is no radial vorticity, and again $Ra_{cr} = O(Ha^2)$ for $Ha \gg 1$. Third, in experimental studies of Rayleigh–Bénard instabilities in vertical cylinders with an electrically insulating vertical wall and with a strong vertical magnetic field, the absence of a measurable temperature perturbation in the central region, particularly near the centreline, may not indicate the absence of the instability. Temperature perturbations arise from the vertical velocity inside the parallel layer and decay as they diffuse radially inward into the core. As Ha is increased, the value of m for the critical mode increases, so that the form of the perturbation temperature (7b) indicates that the radial decay rate increases. Azimuthal voltage variations at the vertical wall would probably be a more sensitive indicator of this instability for strong magnetic fields, since they arise from blocking the radial current.

We introduce $Ra = \gamma Ha^{3/2}$, where γ is an $O(1)$ parameter, i.e. independent of Ha for $Ha \gg 1$. To scale the perturbation variables in all four subregions, we specify that $v_{z1} = O(1)$ inside the parallel layer. The linear perturbation problem, (5), (1a)–(1e) and (6), admits two independent families of solutions: (i) symmetric modes in which v_{z1}, T_1 and j_{z1} are even functions of z, while v_{r1}, $v_{\theta1}$, p_1, j_{r1}, $j_{\theta1}$ and ϕ_1 are odd functions of z, and (ii) antisymmetric modes in which v_{z1}, T_1 and j_{z1} are odd functions of z, while v_{r1}, $v_{\theta1}$, p_1, j_{r1}, $j_{\theta1}$ and ϕ_1 are even functions of z. For every case we have treated with the fully numerical, hybrid or asymptotic approach, the critical mode was a symmetric mode. This agrees with the results of Touihri *et al.* (1999b) and it makes physical sense. For simplicity, we only present the equations for the symmetric modes in the asymptotic solution.

In the core, ϕ_1 and j_{z1} are $O(Ha^{-3})$,

$$T_1 = Ha^{-1/2} T_{1c}(r,z) + Ha^{-1} \hat{T}_{1c}(r,z), \tag{18a}$$

$$p_1 = Ha\, p_{1c}(r,z), \quad p_{1c} = \gamma \int_0^z T_{1c}(r,z^*)\, dz^*, \tag{18b,c}$$

$$v_{r1} = -j_{\theta1} = -Ha^{-1} \frac{\partial p_{1c}}{\partial r}, \quad v_{z1} = -\gamma Ha^{-1} T_{1c}, \tag{18d,e}$$

$$v_{\theta1} = j_{r1} = -Ha^{-1} \frac{m}{r} p_{1c}, \tag{18f}$$

where $T_{1c}(r,z)$ is an even function of z which is governed by

$$\frac{\partial^2 T_{1c}}{\partial r^2} + \frac{1}{r} \frac{\partial T_{1c}}{\partial r} - \frac{m^2}{r^2} T_{1c} + \frac{\partial^2 T_{1c}}{\partial z^2} = 0, \tag{19}$$

and the boundary condition, $T_{1c} = 0$, at $z = b$. The separation-of-variables solution

is

$$T_{1c} = \sum_{N=0}^{\infty} D_N I_m(\alpha_N r) \cos(\alpha_N z), \quad \alpha_N = \left(N + \tfrac{1}{2}\right)\frac{\pi}{b}, \tag{20a,b}$$

where I_m is the modified Bessel function of the first kind and mth order and the coefficients D_N will be determined by matching the core and parallel layer.

In the parallel layer,

$$T_1 = Ha^{-1/2} T_{1c}(1,z) + Ha^{-1} T_{1p}(\xi,z), \quad v_{z1} = v_{z1p}(\xi,z), \tag{21a,b}$$

$$p_1 = Ha\left[\gamma \int_0^z T_{1c}(1,z^*)\,\mathrm{d}z^* + p_{1p}(\xi,z)\right], \quad \phi_1 = Ha^{-1/2}\phi_{1p}(\xi,z), \tag{21c,d}$$

$$v_{r1} = Ha^{-1/2}\left[m\phi_{1p} - \frac{\partial p_{1p}}{\partial \xi}\right], \quad v_{\theta 1} = \frac{\partial \phi_{1p}}{\partial \xi}, \tag{21e,f}$$

$$j_{r1} = Ha^{-1}\left[\frac{\partial^3 \phi_{1p}}{\partial \xi^3} - mp_{1p} - m\gamma \int_0^z T_{1c}(1,z^*)\,\mathrm{d}z^*\right], \tag{21g}$$

$$j_{\theta 1} = Ha^{-1/2}\frac{\partial p_{1p}}{\partial \xi}, \quad j_{z1} = -Ha^{-1/2}\frac{\partial \phi_{1p}}{\partial z}. \tag{21h,i}$$

The equations governing v_{z1p}, p_{1p}, ϕ_{1p} and T_{1p} are

$$\frac{\partial^2 p_{1p}}{\partial \xi^2} = \frac{\partial v_{z1p}}{\partial z}, \quad \frac{\partial p_{1p}}{\partial z} = \frac{\partial^2 v_{z1p}}{\partial \xi^2}, \tag{22a,b}$$

$$\frac{\partial^4 \phi_{1p}}{\partial \xi^4} = \frac{\partial^2 \phi_{1p}}{\partial z^2}, \quad \frac{\partial^2 T_{1p}}{\partial \xi^2} = -\frac{v_{z1p}}{2b}. \tag{22c,d}$$

The boundary conditions (16) become

$$m\phi_{1p} - \frac{\partial p_{1p}}{\partial \xi} = \frac{\partial \phi_{1p}}{\partial \xi} = v_{z1p} = \frac{\partial T_{1p}}{\partial \xi} = 0 \quad \text{at} \quad \xi = 0, \tag{23a–d}$$

$$\frac{\partial^3 \phi_{1p}}{\partial \xi^3} - mp_{1p} = m\gamma \int_0^z T_{1c}(1,z^*)\,\mathrm{d}z^* \quad \text{at} \quad \xi = 0. \tag{23e}$$

The Hartmann conditions (8) for the secondary Hartmann layer become

$$v_{z1p} = \frac{\partial \phi_{1p}}{\partial z} - \frac{\partial^2 \phi_{1p}}{\partial \xi^2} = 0 \quad \text{at} \quad z = b, \tag{24a,b}$$

so that the Hartmann current is important, but the Hartmann pumping is not. Matching the parallel-layer and core solutions gives

$$v_{z1p} \to 0, \quad p_{1p} \to 0, \quad \phi_{1p} \to 0 \quad \text{as} \quad \xi \to -\infty, \tag{25a–c}$$

$$T_{1p} \to \xi \frac{\partial T_{1c}}{\partial r}(1,z) + \hat{T}_{1c}(1,z) \quad \text{as} \quad \xi \to -\infty. \tag{25d}$$

The matching of the $O(Ha^{-1/2})$ temperatures in the core and parallel layer has already been used in (21a), while (25d) comes from matching the $O(Ha^{-1})$ temperatures in the core and parallel layer. In this 2-inner, 2-outer matching, r in the core temperature

(18a) is replaced by $(1 + Ha^{-1/2}\xi)$, and a Taylor series is used to obtain the proper asymptotic form with powers of Ha times functions which are independent of Ha.

The separation-of-variables solution for equations (22a) and (22b), with the boundary conditions (23c), (24a), (25a) and (25b), is

$$v_{z1p} = \sum_{N=0}^{\infty} A_N \exp(\tau_N \xi) \sin(\tau_N \xi) \cos(\alpha_N z), \tag{26a}$$

$$p_{1p} = \sum_{N=0}^{\infty} A_N \exp(\tau_N \xi) \cos(\tau_N \xi) \sin(\alpha_N z), \tag{26b}$$

where $\tau_N = (\alpha_N/2)^{1/2}$. The integral of (22d) with (23d) and (25d) gives

$$\frac{\partial T_{1c}}{\partial r}(1, z) = \frac{1}{2b} \int_{-\infty}^{0} v_{z1p}(\xi, z)\, \mathrm{d}\xi, \tag{27}$$

which reflects the fact that an upward or downward jet inside the parallel layer rejects heat into the core or absorbs heat from the core, respectively. Substitution of (20a) and (26a) into (27) determines D_N in terms of A_N,

$$D_N = Q_N A_N, \tag{28a}$$

$$Q_N = (4b\tau_N)^{-1} \left[m I_m(\alpha_N) - \alpha_N I_{(m-1)}(\alpha_N) \right]^{-1}. \tag{28b}$$

There is no separation-of-variables solution for ϕ_{1p} because of the boundary condition (24b). Walker, Ludford & Hunt (1972) superimposed Greens functions for the operators $(\partial/\partial z \pm \partial^2/\partial \xi^2)$ in order to construct a solution of (22c) with the boundary conditions (23b), (24b) and (25c). Here their solution becomes

$$\phi_{1p} = \int_{-b}^{b} F(z^*) \left\{ \frac{\xi}{2} \operatorname{erf}\left[\frac{\xi}{2}|z - z^*|^{-1/2} \right] + \pi^{-1/2}|z - z^*|^{1/2} \exp\left[-\frac{\xi^2}{4}|z - z^*|^{-1} \right] \right\} \mathrm{d}z^*, \tag{29a}$$

$$F(z) = \frac{\partial^3 \phi_{1p}}{\partial \xi^3}(0, z), \tag{29b}$$

where F is an odd function of z. Substitution of (20a), (26b) and (28) into (23e) gives $F(z)$ in terms of A_N,

$$F = m \sum_{N=0}^{\infty} A_N \left[1 + \frac{Q_N}{\alpha_N} \gamma I_m(\alpha_N) \right] \sin(\alpha_N z). \tag{30}$$

Finally the substitution of (26b), (29) and (30) into the last boundary condition (23a) gives a set of homogeneous linear algebraic equations for A_N,

$$2b^{3/2}m^2\pi^{-1/2} \sum_{N=0}^{\infty} \left[1 + \frac{Q_N}{\alpha_N} \gamma I_m(\alpha_N) \right] S_{KN} A_N - \tau_K A_K = 0, \tag{31}$$

for $K = 0$ to ∞, where

$$S_{KN} = \int_{0}^{1} \int_{0}^{1} \sin[(K + 0.5)\pi Z] \sin[(N + 0.5)\pi Z^*][|Z - Z^*|^{1/2} - (Z + Z^*)^{1/2}]\, \mathrm{d}Z^*\, \mathrm{d}Z. \tag{32}$$
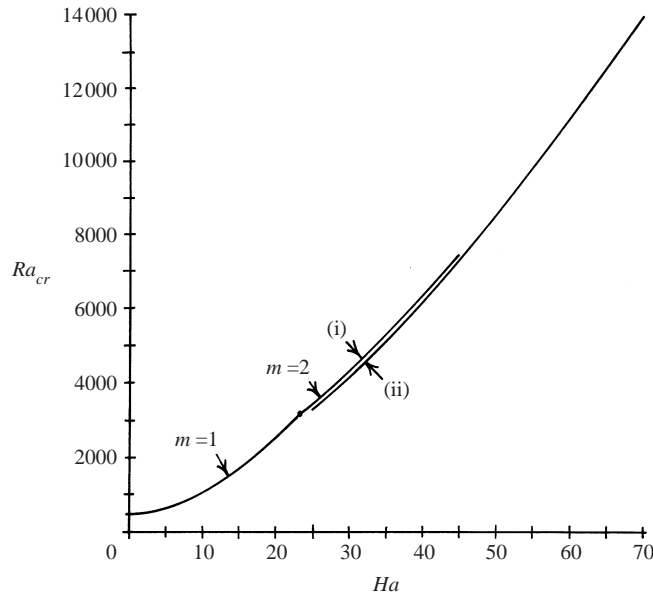
FIGURE 2. Ra_{cr} versus Ha for $b = 1$ and $0 \leqslant Ha \leqslant 70$: (i) fully numerical solution and (ii) hybrid solution. Switch from $m = 1$ to $m = 2$ occurs at $Ha = 23$ and $Ra_{cr} = 3120$.

We truncated both K and N at the value NT, and we numerically evaluated the two integrals in (32) with at least twenty points between adjacent zeros of $\sin[(NT + 0.5)\pi Z]$. Since we have already set $\lambda = 0$, we found the critical value of $\gamma = RaHa^{-3/2}$ for each combination of b and m by increasing γ until the determinant of the coefficient matrix in (31) was zero.

3. Results

We present results for $b = 1.0$ and $b = 0.5$. For our fully numerical solution, our finest grid had 17 Gauss–Lobatto collocation points for $0 \leqslant r \leqslant 1$ and 19 Gauss–Lobatto collocation points for $0 \leqslant z \leqslant b$. For the hybrid solution, our finest grid had 23 points for $0 \leqslant r \leqslant 1$ and 15 points for $0 \leqslant z \leqslant b$. The hybrid solution requires fewer points in the z-direction since numerical resolution of the Hartmann layer at $z = b$ is not needed, but it requires more points in the r-direction in order to achieve numerical resolution of the parallel layer at $r = 1$ for $Ha \leqslant 500$. The same grids were used for both the symmetric and antisymmetric modes, and the critical mode was a symmetric mode for every case considered here. We carried out grid-refinement studies to ensure that the numerical error in the critical Rayleigh number was less than 1% for our finest grid for both the fully numerical and hybrid solutions.

For our fully numerical solution, we found that the upper limit on Ha for numerical accuracy with our finest grid depended on b. In every case, the value of Ra_{cr} decreased as the grid was refined. For $b = 1$, the upper limit was roughly $Ha = 40$, but we also treated $Ha = 45$ where the error in Ra_{cr} is slightly larger than 1%. The ratio of the Hartmann layer thickness to the height of the cylinder varies as b^{-1}, so that better resolution is achieved with a given number of axial collocation points as b is decreased. For $b = 0.5$, the upper limit for numerical accuracy was roughly $Ha = 75$, but we also treated $Ha = 80$, where the error was also slightly more than 1%.

For $b = 1$, the results for Ra_{cr} from the fully numerical solution are plotted for $0 \leqslant Ha \leqslant 45$ and those from the hybrid solution are plotted for $25 \leqslant Ha \leqslant 70$ in
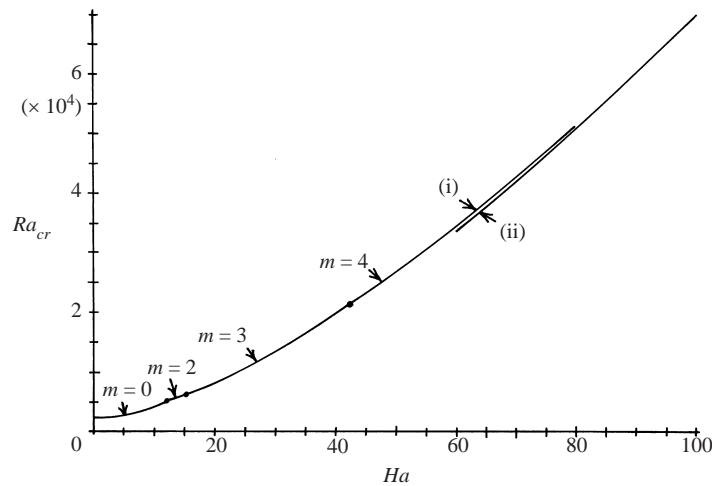
FIGURE 3. Ra_{cr} versus Ha for $b = 0.5$ and $0 \leqslant Ha \leqslant 100$: (i) fully numerical solution and (ii) hybrid solution. Switches from $m = 0$ to $m = 2$ occur at $Ha = 12$ and $Ra_{cr} = 4938$, from $m = 2$ to $m = 3$ at $Ha = 15$ and $Ra_{cr} = 6166$, and from $m = 3$ to $m = 4$ at $Ha = 42$ and $Ra_{cr} = 21\,300$.

figure 2. The fully numerical results for $0 \leqslant Ha \leqslant 15$ agree very well with the results in figure 3 of Touihri *et al.* (1999*b*), after the change from diameter to radius in the definitions of Ra and Ha. As Ha is increased, the critical mode switches from $m = 1$ to $m = 2$ at $Ha = 23$ and $Ra_{cr} = 3120$, while $m = 2$ for the hybrid solution for $b = 1$ and for $25 \leqslant Ha \leqslant 500$. The difference between the fully numerical and hybrid results for Ra_{cr} decreases from 2.6% for $Ha = 25$ to 1.1% for $Ha = 45$. The grid-independence studies showed that any residual numerical error in the fully numerical solution is an overestimation of Ra_{cr}. While the hybrid solution has a tiny numerical error for these small values of Ha, it has an intrinsic $O(Ha^{-1})$ error. We expect this error to lead to an underestimation of Ra_{cr} because the viscous term $\partial^2 \boldsymbol{v}_1 / \partial z^2$ is assumed to be negligible outside the Hartmann layers. With its underestimation of viscous dissipation, we expect the hybrid solution to predict instability at a lower value of Ra_{cr}. For $b = 1$, we conclude that the hybrid solution gives good results for $Ha = 45$. Its accuracy increases as Ha is increased from 45 and its intrinsic $O(Ha^{-1})$ error decreases, until its numerical accuracy deteriorates because the parallel layer is not adequately resolved with our finest grid.

For $b = 0.5$, the results for Ra_{cr} from the fully numerical solution are plotted for $0 \leqslant Ha \leqslant 80$ and those from the hybrid solution are plotted for $60 \leqslant Ha \leqslant 100$ in figure 3. For $b = 0.5$ and $Ha = 0$, the critical mode with $m = 0$ involves a transition from a stagnant fluid to an axisymmetric steady convection (Touihri *et al.* 1999*a*). As Ha is increased, m for the critical mode switches from 0 to 2 at $Ha = 12$ and $Ra_{cr} = 4938$, from 2 to 3 at $Ha = 15$ and $Ra_{cr} = 6166$, and from 3 to 4 at $Ha = 42$ and $Ra_{cr} = 21\,300$, while $m = 4$ for the hybrid solution for $60 \leqslant Ha \leqslant 500$. The difference between the fully numerical and hybrid results for Ra_{cr} decreases from 1.8% for $Ha = 60$ to 1.2% for $Ha = 80$.

For the hybrid solution, we found that the upper limit on Ha for numerical accuracy with our finest grid had a weaker dependence on b than the fully numerical solution. For $b = 1$, grid-independence studies indicated that the error in Ra_{cr} with our finest grid was less than 1% for $Ha \leqslant 500$. The thickness of the parallel layer varies as $(b/Ha)^{1/2}$, so that it becomes thinner as b is decreased. For $b = 0.5$, our finest
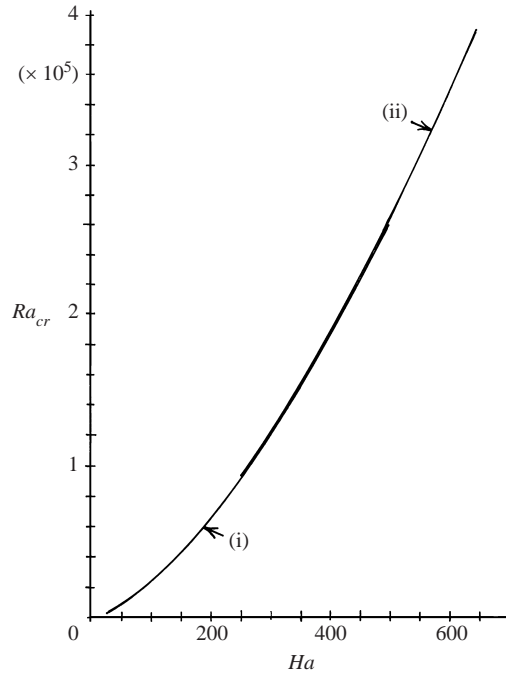
FIGURE 4. Ra_{cr} versus Ha for $b = 1$ and $25 \leqslant Ha \leqslant 650$: (i) hybrid solution and (ii) asymptotic solution.

grid gave accurate results for $Ha \leqslant 400$. For $400 \leqslant Ha \leqslant 500$, the hybrid solution continues to indicate that $m = 4$ for the critical mode, but the possible numerical error in Ra_{cr} is comparable to the small difference between the values of Ra_{cr} for the $m = 4$ and $m = 5$ modes. The Ra_{cr} for $m = 0$ to 3 and $m \geqslant 6$ are all much larger.

For $b = 1$, the asymptotic solution gives $\gamma_{cr} = 23.48183$ for $m = 2$, with significantly higher values for other values of m. Thus we conclude that $m = 2$ for the critical mode for $23 \leqslant Ha \leqslant \infty$. For $b = 1$, the results for Ra_{cr} from the hybrid solution are plotted for $25 \leqslant Ha \leqslant 500$ and those from the asymptotic solution with $Ra_{cr} = 23.48183 Ha^{3/2}$ are plotted for $250 \leqslant Ha \leqslant 650$ in figure 4. For $250 \leqslant Ha \leqslant 500$, the difference between the hybrid and asymptotic results is less than 1.4%. Thus we conclude that the asymptotic solution gives accurate results for $Ha \geqslant 250$. Its accuracy increases as Ha is increased and its $O(Ha^{-1/2})$ intrinsic error decreases. Numerical accuracy is never a problem for the asymptotic solution, so it gives accurate results for any larger value of Ha.

For $b = 0.5$, the asymptotic solution gives $\gamma_{cr} = 67.748044$ for $m = 5$ and $\gamma_{cr} = 68.253627$ for $m = 4$, with much larger values of γ_{cr} for $m = 0$ to 3 and $m \geqslant 6$. For $b = 0.5$, the results for Ra_{cr} from the hybrid solution are plotted for $45 \leqslant Ha \leqslant 500$ and those from the asymptotic solution with $Ra_{cr} = 67.748044 Ha^{3/2}$ are plotted for $400 \leqslant Ha \leqslant 600$ in figure 5. For $400 \leqslant Ha \leqslant 500$, the difference between the results of the hybrid solution for $m = 4$ and the asymptotic solution for $m = 5$ is less than 0.5%. The asymptotic solution indicates that $m = 5$ for the critical mode for $b = 0.5$ and $Ha \gg 1$, and this is confirmed by solutions with $NT = 100$, 200 and 300, but it also indicates that the $m = 4$ mode is very close for $Ha \gg 1$. The hybrid solution indicates that the critical mode has $m = 4$ for $Ha \leqslant 500$, but the difference between the values of Ra_{cr} for the $m = 4$ and $m = 5$ modes is comparable to the possible
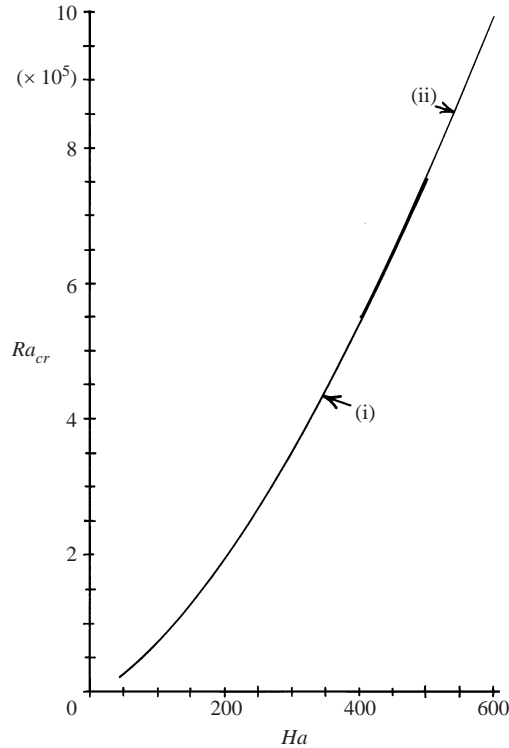
FIGURE 5. Ra_{cr} versus Ha for $b = 0.5$ and $45 \leqslant Ha \leqslant 600$: (i) hybrid solution and (ii) asymptotic solution.

numerical error in Ra_{cr} for $Ha > 400$. Clearly there is a switch from the $m = 4$ mode to the $m = 5$ mode for some value of $Ha > 400$, while the value of Ha and Ra_{cr} is not defined by the present analysis. Nevertheless this difference appears to be moot since both solutions indicate that, as Ra is increased for $Ha > 400$, the $m = 4$ and $m = 5$ modes appear almost simultaneously, while all other modes do not appear until significantly higher values of Ra.

As noted previously, we expect the hybrid solution to underestimate Ra_{cr} because it neglects the axial viscous term outside the Hartmann layers. The asymptotic solution neglects various viscous terms in all four subregions, but it also neglects convective heat transfer outside the parallel layer. An underestimation of convective heat transfer would lead to an overestimation of Ra_{cr}. It is not clear whether the overestimation of Ra_{cr} due to the neglect of convective heat transfer outside the parallel layer or its underestimation due to the neglect of various viscous terms dominates for the asymptotic solution, but the underestimation of convective heat transfer in the asymptotic solution helps explain why the asymptotic values in figures 4 and 5 are higher than the hybrid ones.

For the hybrid solution for $b = 1$, $Ha = 500$, $Ra_{cr} = 258\,920$ and $m = 2$, contour plots of several perturbation variables are presented in figure 6. We normalized the hybrid solution with $v_{z1} = r^m$ at $r = 0.90963$ and $z = 0$. With real modal functions in (4),

$$T = -0.5z + Pr\,\varepsilon \cos(2\theta)T_1(r, z), \quad v_r = \varepsilon \cos(2\theta)v_{r1}(r, z), \tag{33a, b}$$

$$v_z = \varepsilon \cos(2\theta)v_{z1}(r, z), \quad v_\theta = -\varepsilon \sin(2\theta)v_{\theta 1}(r, z). \tag{33c, d}$$
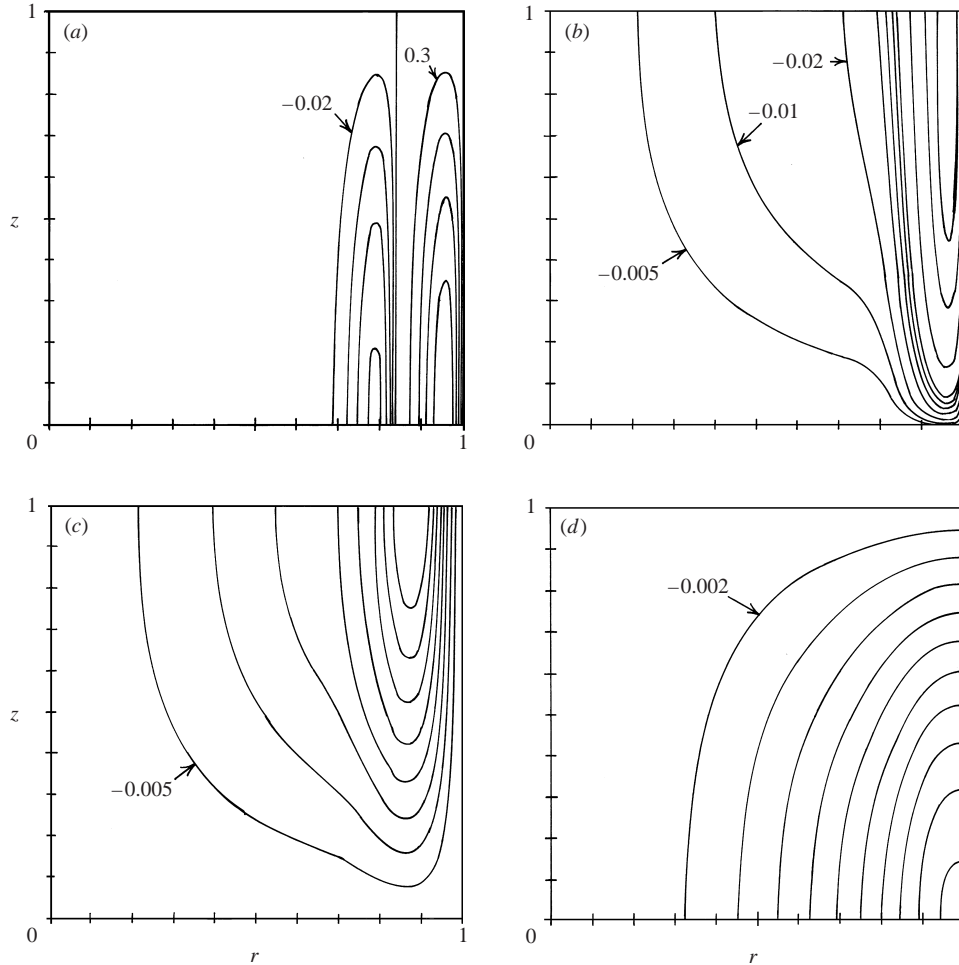
FIGURE 6. Contour plots for the hybrid solution for $b = 1$, $Ha = 500$, $Ra_{cr} = 258\,920$ and $m = 2$. (a) $v_{z1} = -0.02k$ for $k = 0$ to 4 and $v_{z1} = 0.3k$ for $k = 1$ to 4. (b) $v_{\theta1} = -0.005$ and -0.01, $v_{\theta1} = -0.02k$ for $k = 1$ to 5 and $v_{\theta1} = -0.2k$ for $k = 1$ to 3. (c) $v_{r1} = -0.005k$ for $k = 1$ to 8. (d) $T_1 = 0.002k$ for $k = 0$ to 10.

Therefore there is no flow across the planes at $\theta = 0$, $\pm\pi/2$ and π, and the flow in the other three quadrants is given by the reflection of the flow in the first quadrant, $0 \leqslant \theta \leqslant \pi/2$.

Positive values of v_{z1} in figure 6(a) represent upward flow for $0 < \theta < \pi/4$ and downward flow for $\pi/4 < \theta < \pi/2$. The negative values of $v_{\theta1}$ in figure 6(b) represent flow in the positive θ-direction across the plane at $\theta = \pi/4$. The negative values of v_{r1} in figure 6(c) represent radially inward flow for $0 < \theta < \pi/4$ and radially outward flow for $\pi/4 < \theta < \pi/2$. For all critical modes v_{z1} is an even function of z, while v_{r1} and $v_{\theta1}$ are odd functions of z. For $0 < \theta < \pi/4$, there is an upward jet for $0.84 < r < 1$ in figure 6(a), and this jet splits into three separate circulations. First, more than 90% of this upward jet near $r = 1$ for $0 < \theta < \pi/4$ turns to flow in the $+\theta$-direction as the negative values of $v_{\theta1}$ for $0.8 < r < 1$ in figure 6(b). After crossing the $\theta = \pi/4$ plane, this flow turns to become more than 90% of the downward flow for $0.84 < r < 1$ and $\pi/4 < \theta < \pi/2$. The circuit for this flow is completed in $z < 0$. This circulation with
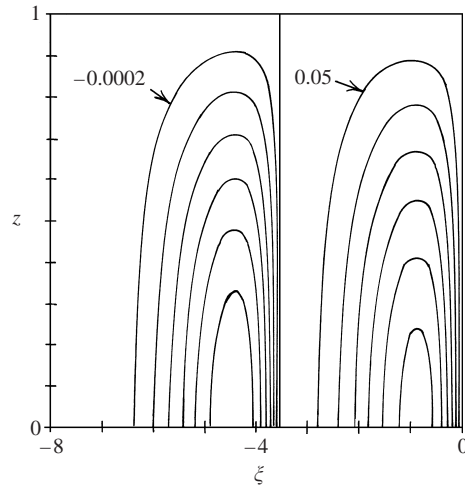
FIGURE 7. Contour plots of v_{z1p} for the asymptotic solution for $b = 1$:
$v_{z1p} = -0.0002k$ for $k = 0$ to 6 and $v_{z1p} = 0.05k$ for $k = 1$ to 6.

more than 90% of the total flow is everywhere nearly tangent to the vertical wall, blocking the radial electric current which would be driven by the interaction of the azimuthal velocity and the axial magnetic field. This is the radial vorticity inside the parallel layer which has relatively small joulean dissipation. Second, roughly 6% of the upward jet for $0.84 < r < 1$ and $0 < \theta < \pi/4$ turns to flow radially inward as the negative values of v_{r1} for $0.7 < r < 1$ in figure 6(c). It then turns to flow downward as the negative values of v_{z1} for $0.68 < r < 0.84$ in figure 6(a), with the circuit completed in $z < 0$. This circulation represents azimuthal vorticity inside the parallel layer, and this vorticity has opposite directions for $0 < \theta < \pi/4$ and for $\pi/4 < \theta < \pi/2$. Third, a few percent of the upward jet for $0.84 < r < 1$ and $0 < \theta < \pi/4$ turns to flow radially into the core as the negative values of v_{r1} for $r < 0.7$ in figure 6(c). This flow turns to cross the $\theta = \pi/4$ plane as the negative values of $v_{\theta 1}$ for $r < 0.7$ in figure 6(b), and then flows radially outward to return to the parallel layer in $\pi/4 < \theta < \pi/2$. This circulation involves axial vorticity in the core.

Contours of T_1 are plotted in figure 6(d). There is no parallel layer here, confirming the asymptotic result that the leading order of T_1 is continuous across the parallel layer. The net upward flow inside the parallel layer rejects heat into the core as it rises to colder levels in the base-state temperature, and this heat rejection produces $T_1 > 0$ for $0 \leqslant \theta \leqslant \pi/4$. The resultant positive buoyancy force inside the parallel layer drives the upward jet. For $\pi/4 \leqslant \theta \leqslant \pi/2$, the net downward flow inside the parallel layer must absorb heat from the core as it descends to hotter levels, thus producing $T_1 < 0$. The resultant negative buoyancy force inside the parallel layer drives the downward jet. Most of the circuit between the upward and downward parallel-layer jets is completed by large values of $v_{\theta 1}$ near the electrically insulated wall at $r = 1$ where the wall blocks the radial electric current which would otherwise produce a body force opposing this azimuthal flow.

For the parallel layer in the asymptotic solution for $b = 1$, $\gamma_{cr} = 23.48183$ and $m = 2$, contours of v_{z1p} are presented in figure 7. We have normalized the asymptotic solution with $A_0 = 1$. The values in figure 7 should be multiplied by 4.5 for comparison to the values in figure 6(a). Clearly the shapes of the contours in figures 6(a) and 7 are the same. The radial scales also agree well. For example, the $v_{z1p} = 0$ contour

at $\xi = -3.55$ in figure 7 coincides perfectly with the $v_{z1} = 0$ contour at $r = 0.84$ in figure 6(a) since $r = 1 + Ha^{-1/2}\xi$. The contours of $v_{\theta 1p}$ agree well with the contours for the larger negative values in figure 6(b), and the contours of T_{1c} agree well with the contours in figure 6(d).

4. Conclusions

We have presented two new solutions for the Rayleigh–Bénard instability in a vertical cylinder with a vertical magnetic field. The hybrid solution combines an analytical solution for the Hartmann layers with a numerical solution for the rest of the liquid domain. The hybrid solution is valid if the Hartmann layers are thin, and it has an intrinsic error which is $O(Ha^{-1})$. The predictions of the hybrid solution agree very well with those of an extension of the fully numerical solution of Touihri *et al.* (1999*b*) for $Ha = 45$ with $b = 1$ and for $Ha = 80$ with $b = 0.5$. The second solution is an asymptotic solution for $Ha \gg 1$ which has an $O(Ha^{-1/2})$ intrinsic error. The asymptotic solution is an analytical solution, and the only numerical step is the evaluation of the determinant of a coefficient matrix in the linear, algebraic equations for the coefficients in one of the separation-of-variables solutions. The predictions of the hybrid and asymptotic solutions agree well for $Ha = 500$. Since the asymptotic solution is valid for all larger values of Ha, the combination of our hybrid solution, our asymptotic solution and the fully numerical solution of Touihri *et al.* (1999*b*) provide accurate results for values of Ha from zero to infinity.

Accurate predictions for higher values of Ha could be obtained from the fully numerical or hybrid solutions by increasing the number of grid points in the axial and radial directions. The very thorough grid-refinement study presented by Prange *et al.* (1999) for the magnetic stabilization of the thermocapillary instability indicates that a large increase in the number of grid points is required for even a small increase in Ha for the fully numerical solution. Therefore it appears to be impractical to extend the fully numerical solution to much higher values of Ha.

The asymptotic solution not only provides accurate results for $Ha \geqslant 500$, it also provides physical insights into the characteristics of the instability with moderately strong magnetic fields. We presented an interpretation of the perturbation variables for the critical mode for $Ha = 500$, $b = 1$ and $m = 2$, but the asymptotic solution provides equally good insights into other flows, such as the instability for $Ha = 200$, $b = 0.5$ and $m = 4$. For all moderately large values of Ha, the only significant convective heat transfer is confined to the parallel layer, and the local upward or downward jet leads to a heat rejection into the core or to a heat absorption from the core, respectively. These heat transfers into or out of the core produce the perturbation temperature in the core. The continuity of this core temperature across the parallel layer provides the buoyancy forces to drive the upward and downward jets. Since the temperature in the core is important in this coupling, the azimuthal scale of the perturbation must remain comparable to the radial and axial dimensions of the core. Therefore m does not increase much as Ha is increased, namely from 1 to 2 for $b = 1$ and from 0 to 5 for $b = 0.5$. This result contrasts with thermocapillary instability with a magnetic field parallel to the free surface. There all perturbation variables are zero outside the parallel layer, and the azimuthal wavelength of the perturbation is comparable to the radial scale of the parallel layer, i.e. $2\pi/m = O(Ha^{-1/2})$ or $m = O(Ha^{1/2})$.

REFERENCES

BAUMGARTL, J. & MÜLLER, G. 1992 Calculations of the effects of magnetic field damping on fluid flow. Comparison of magnetohydrodynamic models of different complexity. *Proc. 8th European Symp. on Materials and Fluid Sciences in Microgravity.* European Space Agency SP-333, p. 161.

BEN HADID, H., HENRY, D. & TOUIHRI, R. 1997 Unsteady three-dimensional buoyancy-driven convection in a circular cylindrical cavity and its damping by magnetic field. *J. Cryst. Growth* **180**, 433.

CHANDRASEKHAR, S. 1961 *Hydrodynamic and Hydromagnetic Stability.* Dover.

DOLD, P. & BENZ, K. W. 1995 Convective temperature fluctuations in liquid gallium in dependence on static and rotating magnetic fields. *Cryst. Res. Technol.* **30**, 1135.

GELFGAT, A. Y. & BAR-YOSEPH, P. Z. 2001 The effect of an external magnetic field on oscillatory instability of convective flows in a rectangular cavity. *Phys. Fluids* **13**, 2269.

HUNT, J. C. R. & LUDFORD, G. S. S. 1968 Three-dimensional MHD duct flows with strong transverse magnetic fields. Part 1. Obstacles in a constant area channel. *J. Fluid Mech.* **33**, 693.

HURLE, D. T. J., JAKEMAN, E. & JOHNSON, C. P. 1974 Convective temperature oscillations in molten gallium. *J. Fluid Mech.* **64**, 565.

JUEL, A., MULLIN, T., BEN HADID, H. & HENRY, D. 1999 Magnetohydrodynamic convection in molten gallium. *J. Fluid Mech.* **378**, 97.

MOREAU R. 1990 *Magnetohydrodynamics.* Kluwer.

NEUMANN, G. 1990 Three-dimensional numerical simulation of buoyancy-driven convection in vertical cylinders heated from below. *J. Fluid Mech.* **214**, 559.

PRANGE, M., WANSCHURA, M., KUHLMANN, H. C. & RATH, H. J. 1999 Linear stability of thermocapillary convection in cylindrical liquid bridges under axial magnetic field. *J. Fluid Mech.* **394**, 281.

TOUIHRI, R., BEN HADID, H. & HENRY, D. 1999a On the onset of convective instabilities in cylindrical cavities heated from below. I. Pure thermal case. *Phys. Fluids* **11**, 2078.

TOUIHRI, R., BEN HADID, H. & HENRY, D. 1999b On the onset of convective instabilities in cylindrical cavities heated from below. II. Effect of a magnetic field. *Phys. Fluids* **11**, 2089.

WALKER, J. S., LUDFORD, G. S. S. & HUNT, J. C. R. 1972 Three-dimensional MHD duct flows with strong transverse magnetic fields. Part 3. Variable-area rectangular ducts with insulating walls. *J. Fluid Mech.* **56**, 121.

WANSCHURA, M., KUHLMANN, H. C. & RATH, H. J. 1996 Three-dimensional instability of axisymmetric buoyant convection in cylinders heated from below. *J. Fluid Mech.* **326**, 399.